

ACTIVE MEDIA

https://doi.org/10.1070/QEL16797

Synthesis and study of $Fe^{2+}:MgAl_2O_4$ ceramics for active elements of solid-state lasers

V.V. Osipov, V.A. Shitov, K.E. Luk'yashin, V.V. Platonov, V.I. Solomonov, A.S. Korsakov, A.I. Medvedev

Abstract. **The results of pioneering studies on preparation of highly transparent $Fe^{2+}:MgAl_2O_4$ ceramics from powders synthesised in a laser torch are presented. This ceramics with a high transparency in the near-IR spectral region is synthesised for the first time at a low temperature (1300 °C) and a short (1 h) sintering time. It is found that, as the iron oxide concentration increases from 0.1 to 5 wt %, the concentration of Fe^{3+} ions in samples decreases to zero. It is shown that the samples of $Fe^{2+}:MgAl_2O_4$ ceramics contain the second phase $(MgO)_{0.91}(FeO)_{0.09}$ with a concentration of several percent, which considerably decreases transmission coefficient T in the visible region. At the same time, the T coefficient increases with increasing wavelength λ due to a decrease in Rayleigh scattering and almost reaches the theoretical value 85.6 % for $\lambda = 4$ μm. The absorption cross section σ for Fe^{2+} ions at $\lambda = 2$ μm is determined to be $(1.66 \pm 0.14) \times 10^{-20}$ cm^2.**

Keywords: *ceramics, spinel, iron, mid-IR region.*

1. Introduction

At present, mid-IR lasing is achieved on transitions of rare-earth ions Er^{3+} ($\lambda = 1.6$ μm), Tm^{3+} ($\lambda = 1.9$ μm), and Ho^{3+} ($\lambda = 2.9$ μm). However, in recent years, particular attention has been paid to longer-wavelength lasers based on transition metal ions Cr^{2+} and Fe^{2+} in different poly- and single crystals, mainly in ZnSe and ZnS [1–10]. This is related to their wide applications, including environment monitoring, detection of remote atmospheric formations, creation of trace gas analysers, optical communications, non-invasive medicine, and some defence applications. This resulted in rather intense development of Cr^{2+} lasers with an average power of up to 140 W [11] and a pulse energy of 1.1 J [12]. The maximum average power of Fe^{2+} lasers achieved to date is 20 W with pulse energies of 10.6 and 7.5 J in the case of cooling with liquid nitrogen and a Peltier element, respectively [8]. Due to a comparatively short lifetime of the upper laser level, the mentioned results were achieved at cryogenic temperatures. The studies in this field are analysed in sufficient detail in [13].

We should also mention studies devoted to the development of room-temperature Fe^{2+} lasers. The pump pulse duration for these lasers must be shorter than the lifetime of the upper laser level, i.e., shorter than 50 ns for ZnS matrices and shorter than 380 ns for ZnSe [13]. This was achieved using a pulsed HF pump laser [14–17]. Peak pump power in a pulsed regime is considerably higher than in a cw mode. In the case of pulsed pumping, the maximum pump power is limited by the appearance of amplified spontaneous noise near the active element surface, where the concentration of Fe^{2+} ions is maximum.

The latter drawback is related to the problems with doping of the mentioned crystals with iron ions, which is performed by thermal diffusion. For example, in works [5, 6], an iron film ~1 μm thick was deposited on the surface of samples of ZnS and ZnSe polycrystals by an ion beam, and then iron ions were embedded into the samples to a depth of ~0.5 μm at a high (800–1250 °C) temperature in vacuum (in [18], at a pressure of 100 MPa). The ion concentration on the surface in this case could reach 10^{19} cm^{-3}. As a result, to prevent parasitic lasing, the pulsed pump beam diameter in [19] did not exceed 4 mm. However, diffusion welding of two iron-doped samples allowed one to increase the active layer thickness, which led to a considerable increase in the maximum pumped region diameter [19]. Thus, the main problems in the development of lasers based on transition metal ions Cr^{2+} and Fe^{2+} are caused by the short lifetime of the upper laser level at room temperature and complicated doping of the mentioned matrices with these ions.

One of the ways to solve these problems is to use highly transparent $MgAl_2O_4$ ceramics as a matrix. In this case, according to the data for the corresponding single crystal [20], the lifetime of the upper laser level $^5T_2$ of the Fe^{2+} ion increases by more than an order of magnitude compared to the lifetime in $Fe^{2+}:ZnSe$ [18], while the use of laser ceramics technology [21] removes the restrictions on the active volume of elements. This approach has been already used to synthesise highly transparent $Co^{2+}:MgAl_2O_4$ ceramics for saturable absorbers in mid-IR lasers. However, the development of these media runs into some problems.

One of the problems of the synthesis of $Fe^{2+}:MgAl_2O_4$ ceramics is related to a rapid escape of magnesium atoms from the samples during sintering due to a high saturated magnesium vapour pressure, which complicates the choice of the compact composition prior to sintering. To decrease the rate of this process, highly transparent ceramics is sintered, as

V.V. Osipov, V.A. Shitov, K.E. Luk'yashin, V.V. Platonov Institute of Electrophysics, Ural Branch, Russian Academy of Sciences, ul. Amundsena 106, 620016 Ekaterinburg, Russia; e-mail: osipov@iep.uran.ru;
V.I. Solomonov, A.I. Medvedev Institute of Electrophysics, Ural Branch, Russian Academy of Sciences, ul. Amundsena 106, 620016 Ekaterinburg, Russia; Ural Federal University named after the First President of Russia B.N. Yeltsin, ul. Mira 19, 620002 Ekaterinburg, Russia;
A.S. Korsakov Ural Federal University named after the First President of Russia B.N. Yeltsin, ul. Mira 19, 620002 Ekaterinburg, Russia

Received 2 September 2018; revision received 9 October 2018
Kvantovaya Elektronika **49** (1) 89–94 (2019)
Translated by M.N. Basieva

a rule, under a pressure by spark plasma sintering [22] or hot isostatic pressing [23]. We know no works the synthesis of highly transparent $Fe^{2+}:MgAl_2O_4$ spinel but cannot exclude that doping with iron ions will be one more problem.

To overcome these difficulties, it is proposed to produce $Fe^{2+}:MgAl_2O_4$ ceramics from nanopowders synthesised in a laser torch. In this case, radicals formed after evaporation of a target material by a laser beam are mixed at a temperature close to the boiling temperature of the materials, while condensation of vapours into nanoparticles occurs at temperatures close to the melting temperature. As was shown previously [24], a high temperature and rapid (for a time shorter than 100 μs) cooling predetermine a high composition homogeneity in the volume. In addition, small sizes of nanoparticles and their narrow size distribution make it possible to decrease the sintering temperature and, therefore, to decrease the escape of magnesium from the samples during sintering.

Thus, the aim of the present study is to study the possibility of creating a new $Fe^{2+}:MgAl_2O_4$ ceramic active element for IR lasers and to study its characteristics.

2. Objects of the study

The $Fe^{2+}:MgAl_2O_4$ nanopowders were synthesised by laser ablation of a target made from coarse Fe_2O_3, MgO, and Al_2O_3 powders with a purity of 99.99% (OOO Lankhit, Moscow). To make the targets, these powders in a required proportion were mixed in a drum mixer with an inclined rotation axis for 48 h. Then, the mixture was uniaxially statically pressed into discs 65 mm in diameter and 15–20 mm thick. Under irradiation by a CO_2 laser with a pulse energy of ~1 J, FWHM duration of ~300 μs, and repetition rate of 500 MHz, the target was evaporated in an atmospheric gas flow. The condensing vapours were first sent to a cyclone separator, in which the largest particles were separated from the flow, and then to a bag filter, where the most part of remained particles precipitated in the air atmosphere. For uniform depletion, the target was rotated and moved in both horizontal and vertical directions. The nanopowder production rate was 19–21 g h^{-1}.

For preparation of $Fe^{2+}:MgAl_2O_4$ ceramics, we synthesised nanopowders with iron oxygen (Fe_3O_4) concentrations of 0.1, 1 and 5 wt%.

The nanopowders were compacted into discs 14.4 mm in diameter and 2–2.5 mm thick by uniaxial static pressing under a pressure of 50–300 MPa or by uniaxial static pressing at p = 16.6 MPa combined with cold isostatic pressing at pressures from 50 to 200 MPa. Independently of the method, the density of compacts was determined only by the applied pressure and varied from 1.52 to 1.93 g cm^{-3}, which corresponded to 41%–52% of the theoretical spinel density (3.72 g cm^{-3}).

The compacts were sintered at a temperature of 1300–1500 °C with a heating rate of 5 K min^{-1} and a cooling rate of 20 K min^{-1}; the exposure time was 1 h. It should be noted that ceramics prepared from compacts obtained from nanopowder under uniaxial static pressures exceeding 100 MPa had isolated radial cracks, while the ceramics made from compacts formed by isostatic pressing were absolutely intact. In the case of compacts pressed from nanopowders preliminarily annealed in an atmospheric furnace at a temperature of 800–1000 °C, the samples remained undamaged up to a pressure of 250 MPa.

The morphological features of synthesised nanopowders were studied using a JEOL JEM 2100 transmission electron microscope (JEOL Ltd, Japan). The phase composition of nanopowders and ceramics was studied using a D8 Discover GADDS X-ray diffractometer (Bruker AXS, Germany). The results were processed using a TOPAS-3 software with Rietveld refinement of structural parameters.

The transmission spectra of ceramics were measured at room temperature in two steps. First, the transmission coefficient in the range of 200--1100 nm was measured on a Shimadzu UV-1700 spectrophotometer (Shimadzu Corp., Japan). The transmission spectra of samples in the long-wavelength region were measured using an IRPrestige-21 Fourier-transform spectrometer (Shimadzu Corp., Japan). The spectrometer range was 1.28–28.5 μm in the case of using a KBr beam splitter, the resolution was 4 cm^{-1}, and the number of background and sample scans was 20. A deuterated L-alanine-doped triglycine sulphate (DLaTGS) detector and a Globar IR source were used. The pulsed cathodoluminescence spectrum of samples was observed using a KLAVI setup [25]. The cathodoluminescence was excited by an electron beam with a duration of 2 ns, an electron energy of 150 keV, and a current density of 60 A cm^{-2}.

3. Results and discussion

Figure 1a shows a transmission electron microscopy image of Fe_3O_4 (1 wt%):$MgAl_2O_4$ nanoparticles from the bag filter. One can see that the particles are slightly agglomerated and have a spherical shape. The size distribution of particles (Fig. 1b) plotted based on such images turned out to be close to a log-normal distribution with an arithmetic mean size of particles of 18.4 nm.

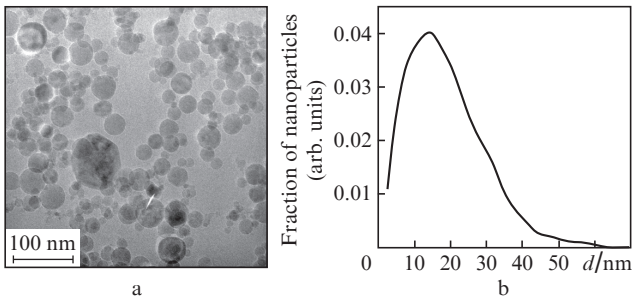

Figure 1. (a) Photograph and (b) size distribution of Fe_3O_4 (1 wt%):$MgAl_2O_4$ nanoparticles.

The X-ray diffraction pattern of the Fe_3O_4 (1 wt%):$MgAl_2O_4$ nanopowder is presented in Fig. 2, and the results of its processing are listed in Table 1 (CSR is the coherent scattering region). These results show that the synthesised powder consists of several phases. The main phase, i.e., spinel ($MgAl_2O_4$), has a cubic structure with the space group Fd3m. The additional phase $(MgO)_{0.91}(FeO)_{0.09}$, whose con-

Table 1. Results of X-ray diffraction analysis of Fe_3O_4 (1 wt%):$MgAl_2O_4$ nanopowders.

Phase composition	Concentration (%)	CSR/nm	Lattice period/Å
Spinel	88 ± 2	12 ± 2	8.084 ± 0.005
$(MgO)_{0.91}(FeO)_{0.09}$	10 ± 2	~7	4.149 ± 0.004
MgO	~2	~32	4.205 ± 0.004

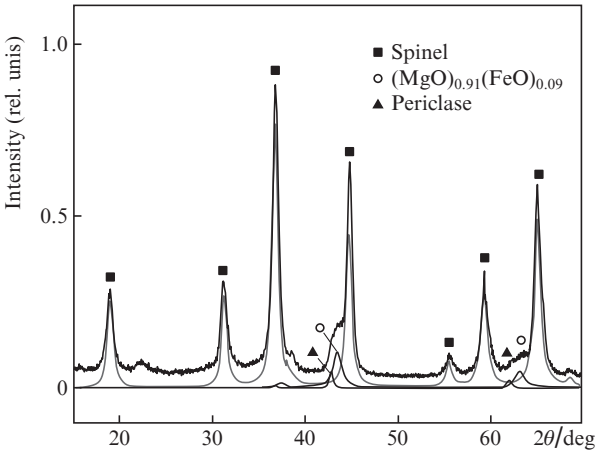

Figure 2. X-ray diffraction pattern of Fe_3O_4 (1 wt%):$MgAl_2O_4$ nanopowder.

centration is 10 wt%, has a cubic structure with the space group Fm3m. In addition, there exists a small amount of MgO (periclase).

Of greatest surprise is the appearance of the second phase $(MgO)_{0.91}(FeO)_{0.09}$ with a high concentration exceeding the concentration of periclase in the nanopowder. Particular attention in the course of the experiments will be paid to the change in the concentrations of these phases during sintering.

Figure 3 shows photographs of aluminium–magnesium spinel ceramic samples with different concentrations of iron, which were synthesised in vacuum at a temperature of 1300 °C for 1 h. The samples are polished, have a thickness of 1.8 m, and vary in colour from colourless to dark brown depending on the iron concentration.

However, when observed in transmission at a particular angle even with the naked eye, the ceramics showed a so-called orange peel structure [26, 27], which can be related to the formation of the second phase. To check this supposition, we performed X-ray diffraction analysis (Fig. 4). The measurements showed that the crystalline component of the material contains the following phases: the main phase $MgAl_2O_4$ (spinel) with the characteristics close to the literature data (PDF No. 00-021-1152, crystal lattice period a = 8.083 Å) and the second (cubic) phase $(MgO)_{0.91}(FeO)_{0.09}$ with the characteristics close to the data of PDF No. 01-077-2365 (a = 4.225 Å).

Analysing the data of Table 2, one should pay attention to the considerable content of the second phase and the small CSRs of the main (210–300 nm) and second (120 nm) phases for all samples. The latter is especially important because

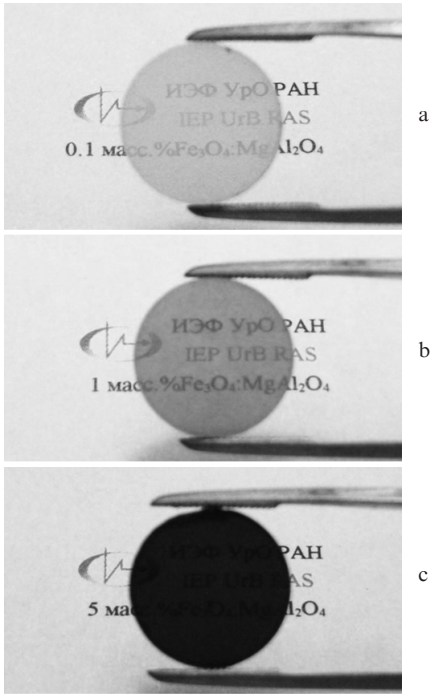

Figure 3. Photographs of (a) Fe_3O_4 (0.1 wt%):$MgAl_2O_4$, (b) Fe_3O_4 (1 wt%):$MgAl_2O_4$, and (c) Fe_3O_4 (5 wt%):$MgAl_2O_4$ spinel samples.

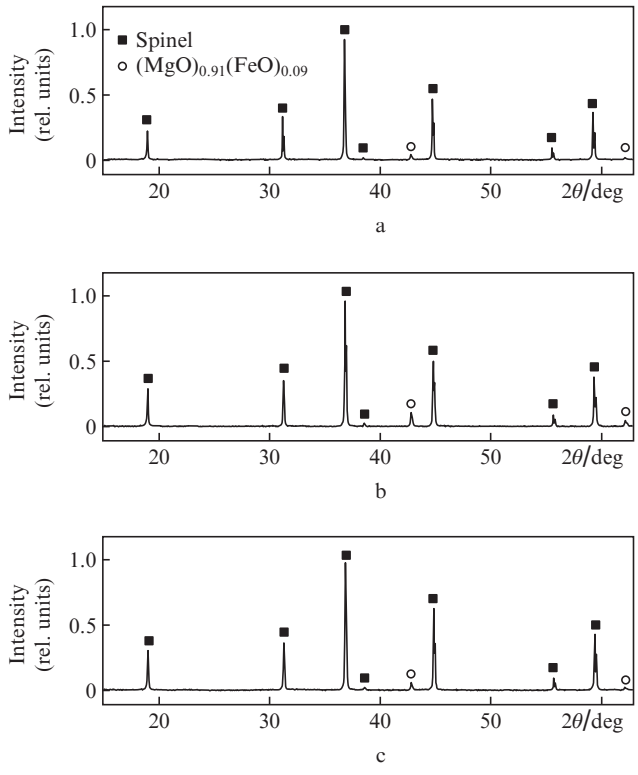

Figure 4. X-ray diffraction patterns of (a) Fe_3O_4 (0.1 wt%):$MgAl_2O_4$, (b) Fe_3O_4 (1 wt%):$MgAl_2O_4$, and (c) Fe_3O_4 (5 wt%):$MgAl_2O_4$ samples.

Table 2. Results of X-ray diffraction analysis of the ceramics.

Sample	Spinel			Second phase		
	Concentration (%)	CSR/nm	Lattice period/Å	Concentration (%)	CSR/nm	Lattice period/Å
Fe_3O_4 (0.1 wt%):$MgAl_2O_4$	97 ± 1	~250	8.086 ± 0.002	3 ± 1	120 ± 10	4.224 ± 0.002
Fe_3O_4 (1 wt%):$MgAl_2O_4$	93 ± 1	~210	8.087 ± 0.002	7 ± 1	116 ± 8	4.223 ± 0.002
Fe_3O_4 (5 wt%):$MgAl_2O_4$	97 ± 1	~300	8.101 ± 0.002	3 ± 1	120 ± 20	4.225 ± 0.002

the inhomogeneity sizes determine which (Rayleigh or Mie) scattering occurs upon propagation of radiation through the sample. The crystal lattice constants increase with increasing concentrations of iron in spinel, which is related to the larger radii of Fe^{2+} and F^{3+} ions compared to Mg^{2+} and Al^{3+}, respectively. The fact that the concentration of the second phase is almost independent of the iron concentration remains unexplainable. This is probably caused by the presence of the MgO phase with almost identical concentrations in all nanopowders and by evaporation of magnesium, which combines with iron and oxygen and forms the second phase, in the process of sintering.

To determine the valence and positions of iron ions in $MgAl_2O_4$, we analysed the luminescence of samples using a KLAVI pulsed cathodoluminescence analyser [25]. The samples with Fe^{3+} should exhibit luminescence corresponding to the $^4T_1(G) \rightarrow {}^6A_1(S)$ optical transition of this ion. According to the Tanabe and Sugano diagrams, which are given, for example, in [28], the luminescence of impurity d ions (i.e., ions with unoccupied d orbital) should occur in the red spectral region. Indeed, the samples with iron oxide concentrations below 1 wt% exhibit a single broad luminescence band in the range of 500–850 nm with the centre at $\lambda = 725$ nm (Fig. 5). It was found that the luminescence intensity in the sample containing 0.1 wt% of Fe_3O_4 exceeds the luminescence intensity in the sample with 1 wt% of Fe_3O_4 by more than two orders of magnitude, while the sample with an iron oxide concentration of 5 wt% exhibited no luminescence in this spectral range.

The observed luminescence band peaking at $\lambda = 725$ nm is unambiguously related to the $^4T_1(G) \rightarrow {}^6A_1(S)$ optical transition of the Fe^{3+} ion substituting the Al^{3+} ion in the octahedral position. The intensity of this band sharply decreases down to zero as the total iron oxide concentration in the samples increases from 0.1 to 5 wt%. A similar effect was previously observed for spinel $Fe^{3+}:ZnAl_2O_4$ in [29], where the photoluminescence intensity of Fe^{3+} ions in octahedral positions decreased with increasing iron concentration in the samples. The authors of [29] related this effect to the transition of Fe^{3+} ions from octahedral to tetrahedral positons, in which Fe^{3+} ions emit a broad band in the range of 400–500 nm. The spectra of the considered samples show no this luminescence band (Fig. 5). Therefore, we should suggest that the decrease in the intensity of the Fe^{3+} spectral band with increasing total iron concentrations in our case is related to a decrease in the absolute concentration of Fe^{3+} ions in the octahedral positions and their complete absence in the samples with 5 wt% of Fe_3O_4. At the total iron oxide concentration exceeding 1 wt %, Fe^{2+} ions mainly substitute Mg^{2+} ions in tetrahedral positions. This is confirmed by the transmission spectra of ceramic samples with different iron concentrations, which are given in Fig. 6. These spectra, like the spectra presented in [30], clearly show a broad (1.5–3.5 μm) absorption band of Fe^{2+} ions in tetrahedral positions, the absorption coefficient of which increases with increasing content of iron in the samples.

From these spectra, we calculated the effective absorption cross section σ of Fe^{2+} ions at $\lambda = 2$ μm by the formula

$$\sigma N + \alpha_s = -\frac{1}{h} \ln \frac{T}{(1-R)^2}, \qquad (1)$$

where $h = 1.8$ mm is the sample thickness, N is the concentration of Fe^{2+} ions in the sample, $R = (n-1)^2/(n+1)^2 \approx 0.068$ is the reflection coefficient of the sample, T is the reflection coefficient, $n = 1.71$ is the ceramics refractive index, and α_s is the scattering coefficient of the ceramics.

From the spectra shown in Fig. 6, it is almost impossible to precisely determine scattering coefficients α_s in the region of $\lambda = 2$ μm due to a strong absorption band in this range. However, it is obvious that $\alpha_s < \sigma N$ for all ceramic samples near $\lambda = 2$ μm. This inequality is most pronounced for ceramic samples with the highest iron oxide concentration (5 wt%). In addition, these samples do not contain trivalent iron ions (Fig. 5), which could distort the obtained results. Because of this, the effective absorption cross section σ was estimated by the transmission spectra of three ceramic samples with the iron oxide concentration of 5 wt% assuming that $\alpha_s = 0$. The iron concentration in these samples was additionally measured by emission analysis to be 3.6 wt%, which well agrees with the Fe_3O_4 content (5 wt%) in the initial mixture. The value of 3.6 wt% corresponds to the iron ion concentration $N = 1.42 \times 10^{21}$ cm^{-3}, with the fraction of iron ions in the second phase not exceeding 1%. Assuming that all iron ions are divalent and neglecting the second phase, the absorption cross section

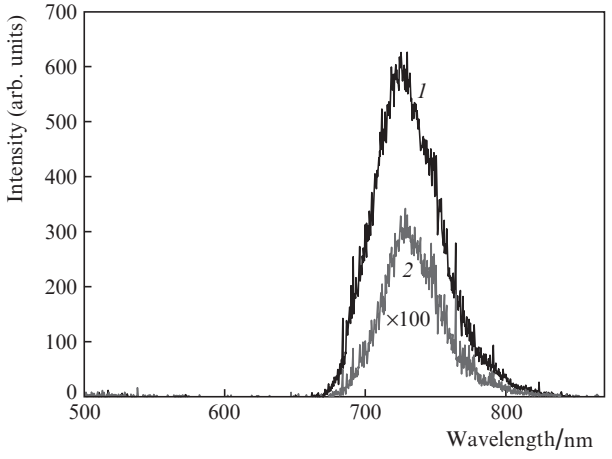

Figure 5. Pulsed cathodoluminescence spectrum of ceramic spinel samples with iron oxide concentrations of (*1*) 0.1 and (*2*) 1 wt%.

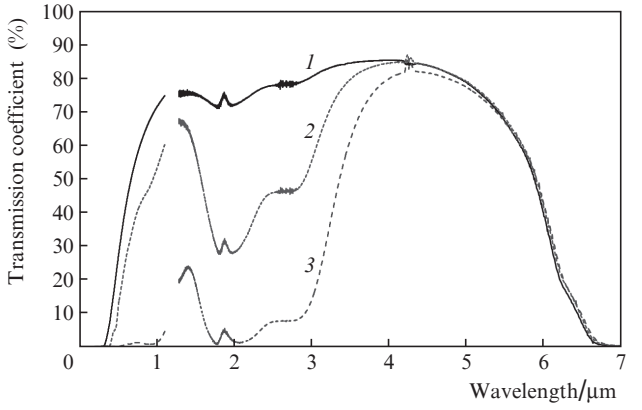

Figure 6. Transmission spectra of aluminium–magnesium spinel ceramics with iron oxide concentrations of (*1*) 0.1, (*2*) 1, and (*3*) 5 wt%.

for $\lambda = 2$ μm was determined to be $\sigma = (1.66 \pm 0.14) \times 10^{-20}$ cm^2. The spread of λ was less than 9%.

The rather low transparency in the spectral region $\lambda < 1$ μm and the existence of the second phase seem to contradict the high transmission coefficient at $\lambda \approx 4$ μm. The latter is close to the theoretical value (86%) and equals 85.6. This result can be explained taking into account that the refractive index at $\lambda = 4$ μm for $MgAl_2O_4$ ($n = 1.6386$ [31]) coincides, with accuracy to two decimal places, with the refractive index of MgO ($n = 1.6681$ [32]), which is the main component of the second phase, while the cross section of Rayleigh scattering by the second-phase crystallites decreases with increasing wavelength proportionally to λ^{-4}.

4. Conclusions

Pioneering studies have been performed on the fabrication of highly transparent Fe^{2+}:$MgAl_2O_4$ ceramics, which can be used for active elements and saturable absorbers of mid-IR lasers. The obtained results are:

– samples of Fe^{2+}:$MgAl_2O_4$ ceramics highly transparent in the mid-IR region are synthesised for the first time;

– transparent spinel is synthesised for the first time at a low (1300 °C) temperature and a short (1 h) sintering time without using spark plasma sintering and high-temperature isostatic pressing;

– the ceramic samples contain, in addition to the main phase, several percent of the second phase $(MgO)_{0.91}(FeO)_{0.09}$;

– the visible luminescence intensity at the $^4T_1(G) \rightarrow {}^6A_1(S)$ transition of the Fe^{3+} ion in the ceramics containing 0.1 wt % of Fe_3O_4 is high, decreases by more than 100 times at the Fe_3O_4 concentration of 1 wt%, and drops to zero at the Fe_3O_4 concentration of 5 wt%, which indicates an increase in the Fe^{2+} concentration with increasing iron concentration in the ceramics;

– the transmission coefficients of the ceramics are relatively small in the visible region, increase with increasing wavelength, and achieve almost the theoretical value 85.6% at $\lambda = 4$ μm. which is caused by the Rayleigh scattering at long wavelengths ($\propto \lambda^{-4}$) and by the close refractive indices of the main and second phases;

– the absorption cross section σ at $\lambda = 2$ μm for Fe^{2+} ions as determined to be $(1.66 \pm 0.14) \times 10^{-20}$ cm^2.

Further investigations will be focused on obtaining phase homogeneity first of all in the nanopowder and then in the ceramics by optimising the sintering regime.

Acknowledgements. This work was supported by State Contract No. 0389-2016-0002 (2018–2020) and the Russian Foundation for Basic Research, Grant No. 17-08-00064.

References

1. Page R.H., Shaffers K.I., DeLoach L.D., Wilke G.D., Patel F.D., Tassano J.B., Payne S.A., Krupke W.F., Chen K.T., Burger A. *IEEE J. Quantum Electron*., **33**, 609 (1997).
2. Sorokina I.T. *Opt. Mater*., **26**, 395 (2004).
3. Klein P.B., Furneaux J.E., Henry R.L. *Appl. Phys. Lett*., **42**, 638 (1983).
4. Adams J.J., Bibeau C., Page R.H., Krol D.M., Furu L.H., Payne S.A. *Opt. Lett*., **24**, 1720 (1999).
5. Demirbas U., Sennaroglu A., Somer M. *Opt. Mater*., **28**, 231 (2006).
6. Kernal J., Fedorov V.V., Gallian A., Mirov S.B., Badikov V.V. *Opt. Express*, **13**, 10608 (2005).
7. Akimov V.A., Voronov A.A., Kozlovskii V.I., Korostelin Yu.V., Landman A.I., Podmar'kov Yu.P., Frolov M.P. *Quantum Electron*., **36**, 299 (2006) [*Kvantovaya Elektron*., **36**, 299 (2006)].
8. Frolov M.P., Korostelin Yu.V., Kozlovsky V.I., Podmar'kov Yu.P., Skasyrsky Yu.K. *Opt. Lett*., **43**, 623 (2018).
9. Grekhem K., Fedorov V.V., Mirov S.B., Doroshenko M.E., Basiev T.T., Orlovskii Yu.V., Osiko V.V., Badikov V.V., Panyutin V.L. *Quantum Electron*., **34**, 8 (2004) [*Kvantovaya Elektron*., **34**, 8 (2004)].
10. Akimov V.A., Voronov A.A., Kozlovskii V.I., Korostelin Yu.V., Landman A.I., Podmar'kov Yu.P., Frolov M.P. *Quantum Electron*., **34**, 912 (2004) [*Kvantovaya Elektron*., **34**, 912 (2004)].
11. Moskalev I., Mirov S., Mirov M., Vasilyev S., Smolski V., Zakrevskiy A., Gapontsev V. *Opt. Express*, **24**, 21090 (2016).
12. Fedorov V.V., Mirov M.S., Mirov S.B., Gapontsev V.P., Erofeev A.V., Smirnov M.Z., Altshuler G.B., in *Frontiers in Optics* (Rochester–New York, USA, 2012) paper FW6B.9.
13. Mirov S.B., Fedorov V.V., Martyshkin D., Moskalev I.S., Mirov M., Vasilyev S. *IEEE J. Sel. Top. Quantum Electron*., **21**, 1601719 (2015).
14. Serafetinides A.A., Rickwood K.R., Papadopoulos A.D. *Appl. Phys. B*, **52**, 46 (1991).
15. Belevtsev A.A., Firsov K.N., Kazantsev S.Y., Kononov I.G. *Appl. Phys. B*, **82**, 455 (2006).
16. Bulaev V.D., Gusev V.S., Kazantsev S.Yu., Kononov I.G., Lysenko S.L., Morozov Yu.B., Poznyshev A.N., Firsov K.N. *Quantum Electron*., **40**, 615 (2010) [*Kvantovaya Elektron*., **40**, 615 (2010)].
17. Velikanov S.D., Domazhirov A.P., Zaretskii N.A., Kazantsev S.Yu., Kononov I.G., Kromin A.A., Podlesnykh S.V., Sivachev A.A., Firsov K.N., Kharitonov S.V., Tsykin V.S., Shchurov V.V., Yutkin I.M. *Quantum Electron*., **45**, 989 (2015) [*Kvantovaya Elektron*., **45**, 989 (2015)].
18. Dormidonov A.E., Firsov K.N., Gavrishchuk E.M., Ikonnikov V.B., Kazantsev S.Yu., Kononov I.G., Kotereva T.V., Savin D.V., Timofeeva N.A. *Appl. Phys. B*, **122**, 211 (2016).
19. Balabanov S.S., Firsov K.N., Gavrishchuk E.M., Ikonnikov V.B., Kazantsev S.Yu., Kononov I.G., Kotereva T.V., Savin D.V., Timofeeva N.A. *Laser Phys. Lett*., **15**, 045806 (2018).
20. Sackuvich R.K., Peppers J.M., Myoung N.S., Badikov V.V., Fedorov V.V., Mirov S.B. *Proc. SPIE*, **8235**, 66 (2012).
21. Ikesue A., Aung Y.L., Lupei V. *Ceramic Lasers* (Cambridge: Cambridge University Press, 2013).
22. Wang C., Zhao Z. *Scr. Mater*., **61**, 193 (2009).
23. Krell A., Hutzler T., Klimke J., Potthoff A. *J. Am. Ceram. Soc*., **93**, 2656 (2010).
24. Osipov V.V., Kotov Yu.A., Ivanov M.G., Samatov O.M., Lisenkov V.V., Platonov V.V., Murzakayev A.M., Medvedev A.I., Azarkevich E.I. *Laser Phys*., **16**, 116 (2006).
25. Mikhailov S.G., Osipov V.V., Solomonov V.I. *Prib. Tekh. Exper*., **3**, 164 (2001).
26. Greskovich C., Chernoch J.P. *J. Appl. Phys*., **44**, 4599 (1973).
27. Bagaev S.N., Osipov V.V., Pestryakov E.V., Solomonov V.I., Shitov V.A., Maksimov R.N., Orlov A.N., Petrov V.V. *Zh. Prikl. Mekh. Tekh. Fiz*., **56**, 180 (2015).
28. Sviridov D.T., Sviridova R.K. *Opticheskie spektry perekhodnykh metallov v kristallakh* (Optical Spectra of Transition Metals in Crystals) (Moscow: Nauka, 1976).

29. Pathak N., Gupta S.K., Sanyal K., Kumar M., Kadam R.M., Natarjan V. *Dalton Trans*., **43**, 9313 (2014).
30. Slack G.A., Ham F.S., Chrenko R.M. *Phys. Rev*., **152**, 376 (1966).
31. Tropf W.J., Thomas M.E. *Handbook of Optical Constants of Solids II* (Orlando: Academic Press, 1991).
32. Stephens R.E., Malitson I.H. *J. Res. Nat. Bur. Stand*., **49**, 249 (1952).